

# Probing Entanglement Scaling Across a Quantum Phase Transition on a Quantum Computer

Qiang Miao,<sup>1</sup> Tianyi Wang,<sup>2</sup> Kenneth R. Brown,<sup>1,3,2,4</sup> Thomas Barthel,<sup>2,1</sup> and Marko Cetina<sup>1,2,3</sup>

<sup>1</sup>*Duke Quantum Center, Duke University, Durham, North Carolina 27701, USA*

<sup>2</sup>*Department of Physics, Duke University, Durham, North Carolina 27708, USA*

<sup>3</sup>*Department of Electrical and Computer Engineering,  
Duke University, Durham, North Carolina 27708, USA*

<sup>4</sup>*Department of Chemistry, Duke University, Durham, North Carolina 27708, USA*

(Dated: December 2024)

The investigation of strongly-correlated quantum matter is challenging due to the curse of dimensionality and complex entanglement structures. This complexity is especially pronounced in the vicinity of continuous quantum phase transitions, where quantum fluctuations occur on all length scales. While quantum simulators give well-controlled access to strongly-correlated systems, the study of critical systems has been hampered by strong finite-size effects caused by diverging correlation lengths, and there has been limited progress on methods to probe many-body entanglement due to restrictions in measurement protocols. We address these challenges by using the multiscale entanglement renormalization ansatz (MERA) and implementing a holographic subsystem tomography on a fully-connected trapped-ion quantum computer. Our method accurately represents infinite systems and long-range correlations with few qubits, enabling the efficient extraction of observables and entanglement properties also at criticality. We observe a quantum phase transitions with spontaneous symmetry breaking and reveal the evolution of entanglement measures across the critical point. For the first time, we demonstrate log-law scaling of subsystem entanglement entropies at criticality on a digital quantum computer. This demonstrates the potential of MERA for a practicable investigation of strongly-correlated many-body systems on quantum computers.

## I. INTRODUCTION

Continuous phase transitions are of great interest in physics and materials science. In the vicinity of such transitions we exhibit *universality*, where long-range properties decouple from microscopic details, and the singular behavior of physical quantities such as susceptibilities, correlation lengths, and correlation times can be characterized by universal critical exponents. Whereas classical phase transitions are driven by thermal fluctuations, quantum phase transitions occur at zero temperature when a system parameter is varied, and the ground state becomes highly entangled due to quantum fluctuations. The distinctive feature of entanglement in the quantum realm endows quantum phase transitions with richer properties, yet also makes them more challenging to explore [1, 2].

Recently, rapid progress on controlled quantum platforms has led to great interest and promise in exploring quantum many-body systems on quantum simulators and computers [3–10]. Previous works [11–18] highlight progress in the experimental characterization of entanglement. However, probing entanglement structures across quantum phase transitions still presents significant challenges. In particular, analog quantum simulators offer large system sizes, but a limited range of models and set of measurable quantities [19]. Digital machines provide the capability to study complex models and probe entanglement but face the following challenges: (i) *Limited number of qubits*: Strictly speaking, quantum phase transitions occur only in infinite systems, and finite-size effects are pronounced in the vicinity of critical points.

A direct preparation of critical ground states requires a huge number of qubits, far beyond the capabilities of current quantum devices. (ii) *Exponential cost for probing subsystem entanglement*: To resolve details about the entanglement structure, one needs tomography for large subsystem sizes. In principle, this is associated with exponential costs for the required classical and quantum resources. (iii) *Difficulties in state preparation*: Without insight into the physics, a vanishing energy gap and correspondingly high entanglement require a highly expressive ansatz to be prepared on digital simulators or a complex preparation scheme on analog simulators. The preparation of a highly expressive ansatz involves a large number of gates, leading to low trainability [20, 21] and considerable accumulated infidelity.

Here, we overcome these challenges for condensed-matter ground states by employing highly structured quantum circuits based on a hierarchical type of tensor network, namely the multiscale entanglement renormalization ansatz (MERA) [22, 23]. This ansatz can naturally represent an infinite system and encode long-range correlations with high accuracy, even at the critical point. Importantly, the causal structure of MERA significantly reduces the total and measured numbers of qubits needed and only requires a logarithmic circuit depth [24–27] such that we can efficiently extract local observables, subsystem entanglement, and entanglement spectra. Furthermore, MERA are resistant to noise [28] and avoid barren plateaus [29, 30].

In this work, we study quantum many-body ground states with high fidelity on a digital quantum computer based on an Ytterbium-ion ( $^{171}\text{Yb}^+$ ) chain. We demon-

strate a quantum phase transition characterized by spontaneous symmetry breaking in the thermodynamic limit, using only up to 12 qubits. We demonstrate universal scaling of relevant physical quantities in the vicinity of the transition and observe significant changes in the structure of entanglement across the critical point. At the critical point, where the correlation length  $\xi$  diverges, we observe a maximum in the single-site entanglement entropy. Our data show that the subsystem entanglement entropy follows a universal log-area law, and the gap in the (renormalized) entanglement Hamiltonian closes with increasing subsystem size. In non-critical regimes, the observed subsystem entanglement entropy follows the expected area law [31–33], and the gap of the (renormalized) entanglement Hamiltonian remains open when increasing the subsystem size. Furthermore, the measured entanglement Hamiltonian correctly reproduces symmetry properties.

## II. SETUP

### A. MERA circuits

Preparing ground states of many-body systems systems can be difficult due to long-range quantum fluctuations. This difficulty can be mitigated by taking into account the entanglement structure. We implement MERA on a quantum computer to approximate the ground state  $|\Psi\rangle$  in the thermodynamic limit. As shown in Fig. 1a, its layered structure introduces a holographic dimension associated with a hierarchy of length and energy scales. The MERA comprises  $T$  layers of isometries and unitary entanglers, which can be implemented efficiently on quantum hardware. Viewed in the order of state preparation (top to bottom), going from layer to layer, the MERA circuit first encodes the longer-range correlations (lower energy scales) and then progressively includes shorter-range correlations (higher energy scales) until reaching the physical layer. Viewed in reverse, MERA acts as a renormalization group flow, systematically removing short-distance entanglement by disentanglers and then coarse-graining by projections at each step until the final layer  $T \sim \log \xi$  is reached, where  $\xi$  is the largest correlation length in the system.

Figure 1a shows a MERA with bond dimension  $\chi = 2$ , corresponding to one qubit per renormalized site. MERA with larger  $\chi$  can be implemented by assigning multiple qubits to each renormalized site and realizing the entanglers as sub-circuits of two-qubit Trotter gates [25, 26].

### B. Observables and holographic subsystem tomography

Experimentally, local observables can be studied by preparing only their causal-cone circuits, e.g., all non-shaded MERA tensors indicated in Fig. 1a for a mea-

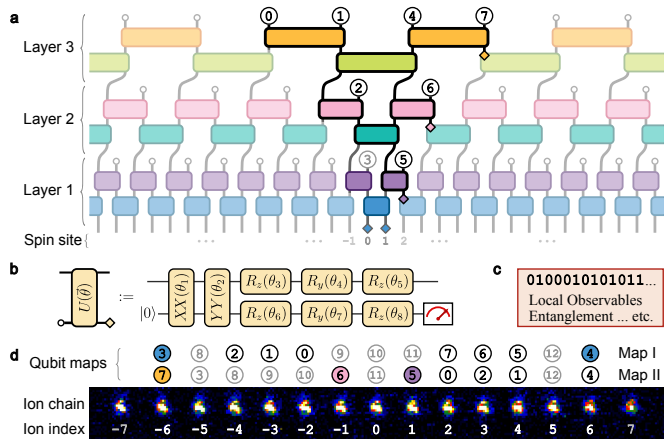


FIG. 1. **Mapping of MERA to a trapped-ion chain.** **a**, An infinite, binary 1D MERA with three homogeneous layers. The ansatz is prepared from top to bottom, with each layer comprising entangling gates and isometries that double the number of sites (boxes with open circles). The output is the many-body state on the physical spin sites. Repeating the shown MERA circuit horizontally in the spatial dimension generates a state in the thermodynamic limit. Local observables and bipartite entanglement can be extracted by executing circuits within the corresponding causal cone (unshaded area) and measuring the target qubits. **b**, For bond dimension  $\chi = 2$ , each MERA tensor corresponds to a sequence of two- and one-qubit native gates with two inputs and two outputs. Open circles indicate qubits initialized in  $|0\rangle$  and diamonds correspond to measurements. **c**, Repeated measurements on a quantum computer yield probabilistic binary outcomes (0s and 1s), from which the desired physical properties can be determined. **d**, Fluorescence image of a 15-ion ( $^{171}\text{Yb}^+$ ) chain with two hardware-tailored examples of ion-to-qubit mappings. Qubit map I is used for local measurement on sites 0 and 1. Map II is optimized for the study of entanglement with respect to a bipartition into the semi-infinite subsystems  $(-\infty, 1]$  and  $[2, \infty)$ .

surement on sites 0 and 1 (qubit map I). The shaded tensors are outside the causal cone and cannot influence the local measurement. To study entanglement entropies and spectra for a spatial bipartition of the system into parts  $A$  and  $B$ , one needs the reduced density matrix for one of the subsystems, say  $\rho_B = \text{Tr}_A |\Psi\rangle\langle\Psi|$ . The advantage of MERA is that we do not need to prepare the state  $|\Psi\rangle$  of the full system to access  $\rho_B$ , but only the causal cone of the *boundary* between  $A$  and  $B$ . This *holographic subsystem tomography* only requires running those gates that generate entanglement between the subsystems. For a bipartition into sites  $A = (-\infty, 1]$  and  $B = [2, \infty)$ , this is indicated by the black-bounded boxes in Fig. 1a (qubit map II). Tomography for the renormalized sites (qubits) that leave the causal cone gives access to  $\rho_B$  (in a nontrivial basis). Due to these causal structures, the required number of qubits and quantum gates scales with the layer number  $T \sim \log \xi$ , rather than the total system size. Details are described in Appx. B.

In the experiment, we implement an infinite, homoge-

neous, binary 1D MERA with bond dimension  $\chi = 2$  and up to  $T = 5$  layers. This ansatz captures a correlation range of approximately  $3 \times 2^5 = 96$  sites. For the self-similar critical systems, the correlation length diverges,  $\xi \rightarrow \infty$ . To address this, we employ a scale-invariant MERA [34] as discussed in below in Sec. III B 2 and Appx. D.

### C. Trapped-ion system

We implement MERA circuits on a digital quantum computer consisting of a linear chain of fifteen individually addressable  $^{171}\text{Yb}^+$  ions. The ions are spaced by approximately  $3.7\ \mu\text{m}$  and are confined in a micro-fabricated Paul trap (Sandia HOA-2.1.1 [35]) held in a room-temperature vacuum chamber (see Fig. 1d). The qubits are encoded in the hyperfine ‘‘clock’’ states of the ground  $^2\text{S}_{1/2}$  electronic manifold of the  $^{171}\text{Yb}^+$  ions as  $|0\rangle \equiv |F = 0; m_F = 0\rangle$  and  $|1\rangle \equiv |F = 1; m_F = 0\rangle$ , where  $F$  is the total atomic angular momentum and  $m_F$  its projection on the magnetic field direction. Qubits are initialized in the  $|0\rangle$  state using optical pumping with a state preparation error of  $10(6) \times 10^{-5}$ . States are measured via state-dependent fluorescence on the 369 nm D1 line, yielding measurement errors of 0.4~0.5% for the bright  $|1\rangle$  state and 0.1~0.2% for the dark  $|0\rangle$  state.

The qubits are manipulated via a Raman process using a wide ( $300\ \mu\text{m} \times 30\ \mu\text{m}$ ) global-addressing laser beam together with equispaced  $1\ \mu\text{m}$ -diameter individual-addressing laser beams derived from the same 355 nm pulsed laser. Available single-qubit operations are virtual  $z$ -axis rotation  $R_z(\theta)$ , implemented via phase offsets in the radio-frequency controls, and a physical rotation gate in the  $x$ - $y$  plane, described by  $R(\theta, \phi) = e^{-i\theta(\hat{X} \cos \phi + \hat{Y} \sin \phi)/2}$ . Entangling gates between arbitrary qubits  $i$  and  $j$ ,  $X_i X_j(\theta) = e^{-i\theta \hat{X}_i \otimes \hat{X}_j / 2}$ , are performed by using the 355 nm Raman process to apply a state-dependent force on the addressed ions to realize a Mølmer-Sørensen interaction using the shared radial motional modes of the ion chain. The all-to-all connectivity of this platform simplifies the implementation of the non-local MERA circuits. The participation of individual ions in different motional modes deterministically affects the errors of different entangling gates as discussed in Appx. A 3; we use this information to optimize the mapping of ions to qubits for each MERA circuit (Fig. 1d).

## III. RESULTS

We apply the MERA approach for the one-dimensional transverse-field Ising model, a paradigmatic system in quantum criticality. The Ising Hamiltonian is given by

$$\hat{H} = - \sum_i^N \hat{X}_i \hat{X}_{i+1} - g \sum_i^N \hat{Z}_i, \quad (1)$$

where  $\hat{X}_i$  and  $\hat{Z}_i$  are the Pauli operators acting on the spin at lattice site  $i$ , and  $g$  controls the relative strength of the transverse field. For  $|g| < 1$  the system is ferromagnetic with nonzero spontaneous magnetization along  $\hat{X}$ , while for  $|g| > 1$  it becomes paramagnetic, favoring alignment with the transverse field and exhibiting zero magnetization. These two phases are separated by a continuous (second-order) quantum phase transition at the critical point  $|g_c| = 1$ . At criticality, the correlation length  $\xi$  diverges as  $\propto |g_c - g|^{-1}$ , and the long-range physics is governed by a conformal field theory (CFT) with central charge  $c = 1/2$ .

The Hamiltonian (1) has a  $\mathbb{Z}_2$  symmetry with respect to the global spin-flip generated by  $\bigotimes_i^N \hat{Z}_i$ , which partitions the eigenstates into even and odd parity sectors. Within a given parity sector, the magnetization  $\langle \hat{X} \rangle$  vanishes since  $\hat{X}$  changes sign under the spin-flip. In the ferromagnetic phase, the ground states in the even and odd sectors approach near-degeneracy when increasing the system size  $N$ . In the thermodynamic limit, this degeneracy becomes exact, and any infinitesimal symmetry-breaking perturbation selects one of the two ground states, yielding a spontaneous magnetization that follows the scaling law [36, 37]

$$\lim_{N \rightarrow \infty} \langle \hat{X} \rangle = \pm (1 - g^2)^{1/8} \quad \text{for } |g| < 1. \quad (2)$$

By contrast, in the paramagnetic phase, the ground state remains unique with even parity. Thus,  $\langle \hat{X} \rangle$  serves as a clear order parameter distinguishing ferromagnet and paramagnet.

Due to its exact solvability and well-characterized critical behavior, the transverse field Ising model is a good testbed. As shown in the following, MERA on a noisy trapped-ion platform accurately captures local observables, local entanglement measures, and subsystem entanglement scaling for the Ising model.

### A. Quantum phase transition

To determine the expectation values  $\langle \hat{O}_i \rangle$  of local observables within the infinite MERA ansatz for the ground state of the Ising model (1), we prepare the causal-cone state of the target spins on the quantum computer (see Fig. 1). The number  $T$  of MERA layers is chosen in the range from 2 to 5 depending on the correlation length, with  $T = 2$  layers far away from criticality and up to 5 layers near the critical point. Correspondingly, the number of required qubits varies from 6 to 12.

Figure 2a shows the measured average magnetization  $\langle \hat{X} \rangle$  in the  $x$ -direction as a function of the  $z$ -field  $g$ . For  $g > 1$ , the observed magnetization is zero within the statistical uncertainty. For  $g < 1$ , we observe nonzero magnetization along the  $x$ -direction, corresponding to the spontaneous breaking of the  $\hat{X} \rightarrow -\hat{X}$  ( $\mathbb{Z}_2$ ) symmetry in the Ising model. The observed magnetization far

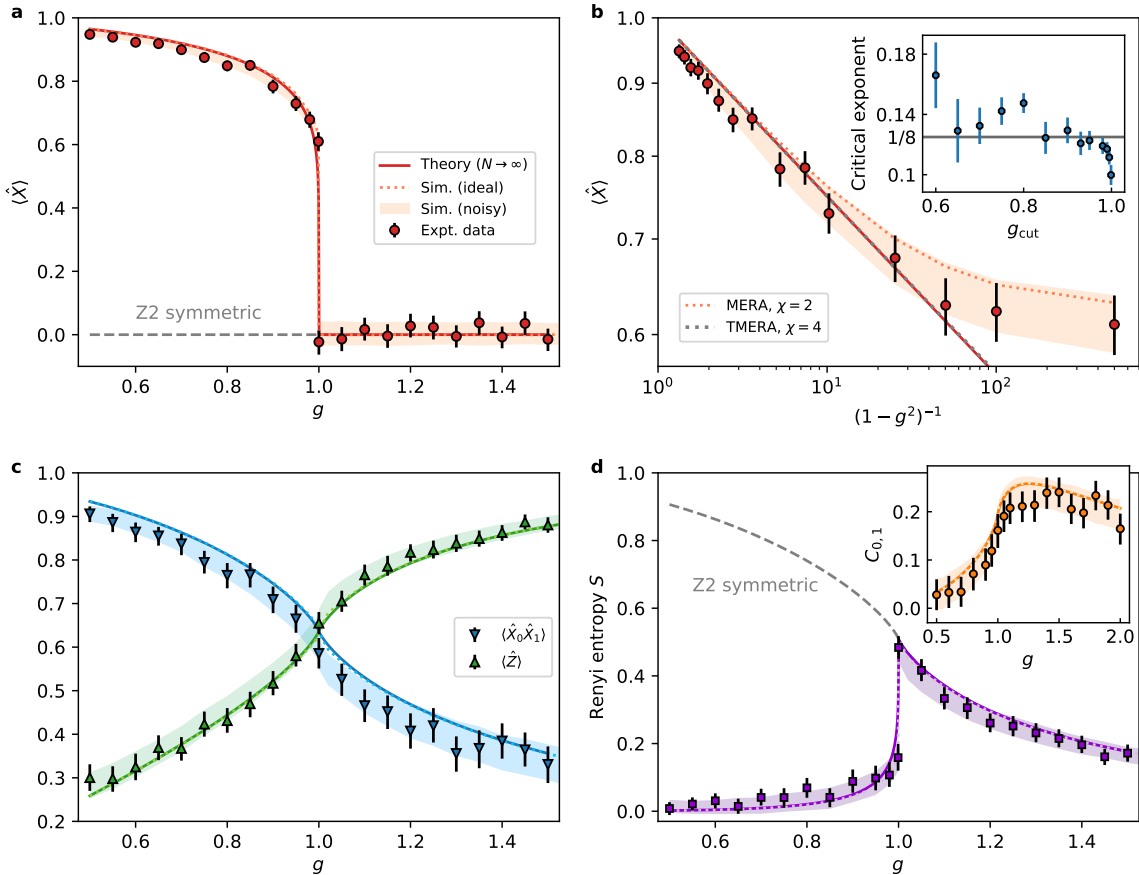


FIG. 2. **Local observables and few-site entanglement in 1D transverse-field Ising model.** **a**, Mean magnetization  $\langle \hat{X} \rangle$  as a function of the transverse field  $g$ . The dashed gray line indicates the reference value for a  $\mathbb{Z}_2$ -symmetric state. **b**, Mean magnetization  $\langle \hat{X} \rangle$  in the  $\mathbb{Z}_2$  symmetry-broken ferromagnetic phase ( $g < 1$ ). The orange (gray) dotted lines corresponds to theoretical predictions for MERA with bond dimension  $\chi = 2$  and Trotterized MERA [25, 26] with  $\chi = 4$ . (Inset) Critical exponent as fitted from the field interval  $g \in [0.5, g_{\text{cut}}]$  with error bars representing  $1\sigma$  fitting uncertainties. The theoretical critical exponent for the Ising class is  $1/8$ . **c**, Further local observables associated with terms in the Ising Hamiltonian (1). **d**, The Rényi-2 entanglement entropy of a single spin. The dashed gray line again indicates the  $\mathbb{Z}_2$ -symmetric reference value. (Inset) The nearest-neighbor concurrence  $C_{0,1}$  (pairwise entanglement) between two neighboring sites. For all plots, solid lines represent theoretical predictions in the thermodynamic limit, dotted lines correspond to ideal infinite MERA simulations, and the shaded areas indicate the central 95% quantile obtained from noisy simulations based on error models that reflect experimental device characteristics. Unless otherwise specified, the error bars indicate 95% confidence intervals obtained from a bootstrap resampling of the experimental data, based on 2,000 measurements per quantum circuit.

away from criticality is slightly lower than the theoretical prediction  $\langle \hat{X} \rangle = (1 - g^2)^{1/8}$  for the thermodynamic limit  $N \rightarrow \infty$ , due to experimental noise.

To account for errors, we conducted separate experiments to characterize the system, and extracted error parameters. We model the effects of addressing noise due to the ions' motion as well as gate-induced dephasing by randomly perturbing gate angles in each shot. We model idle qubit dephasing, state preparation and measurement (SPAM) errors, and  $X$ -flip errors during entangling gates by introducing random  $Z$ - and  $X$ -flips into the simulated circuit. For more details, see Appx. A. As shown in Fig. 2a, the noisy simulations show excellent agreement with the experimental data.

The measured order parameter  $\langle \hat{X} \rangle$  from Fig. 2a near the phase-transition point  $g = 1$  is re-plotted in Fig. 2b on a log-log scale. Due to the small MERA bond dimension  $\chi = 2$ , both the experimental data and numerical simulations saturate around a non-zero value as the system approaches the critical regime. Nevertheless, it is still feasible to extract the critical exponent from these experimental data. The inset shows the critical exponent fitted on varying data ranges  $g \in [0.5, g_{\text{cut}}]$ . The values gradually converge to the theoretical prediction of  $1/8$ , but deviate sharply when  $g_{\text{cut}}$  approaches the critical field  $g = 1$ , highlighting the challenges in this regime. Such deviations near the critical point can be significantly mitigated by increasing the bond dimension of the MERA

circuit. As shown by the thick gray dashed line, a Trotterized MERA circuit [25, 26] with  $\chi = 4$  achieves sufficient accuracy to eliminate these discrepancies, at the cost of requiring more qubits and quantum gates.

Figure 2c shows further local observables in the ground state as functions of the transverse field strength  $g$ . When increasing  $g$ , the dominant contribution to the groundstate energy shifts from the correlator  $\langle \hat{X}_i \hat{X}_{i+1} \rangle$  to the field term  $\langle \hat{Z}_i \rangle$ , and one observes a symmetry between these quantities with respect to the critical point  $g = 1$ . This symmetry is due to Kramers–Wannier duality [38]. In the experiment, we observe that these two observables cross at a slightly smaller  $g$ . These deviations align well with simulations of the noise model. We attribute the downward deviation of  $\langle \hat{X}_0 \hat{X}_1 \rangle$  primarily to dephasing noise, while the slightly upward deviation of  $\langle \hat{Z} \rangle$  is mainly caused by degradation in  $XX$ -gate rotations due to axial motion.

## B. Entanglement structure

In the following, we use MERA to investigate the groundstate entanglement across the quantum phase transition in the transverse-field Ising model (1). We find that MERA on the digital quantum computer can resolve details about the entanglement structure, including the hallmark transition of an area-law to a log-area-law scaling of entanglement entropies when reaching the critical point.

### 1. Local entanglement measures

For a pure state  $|\Psi\rangle$ , the entanglement between subsystem  $B$  and its complement  $A$  can be quantified by the Rényi entanglement entropy

$$S_B^{(\alpha)} = \frac{1}{1-\alpha} \log_2 \text{Tr}(\varrho_B^\alpha), \text{ where } \varrho_B = \text{Tr}_A |\Psi\rangle\langle\Psi| \quad (3)$$

is the reduced density matrix for subsystem  $B$ . While our approach would work for any  $\alpha$ , we focus on the Rényi-2 entropy ( $\alpha = 2$ ) as all Rényi entropies with  $\alpha > 0$  exhibit similar scaling behavior. For a single-site subsystem, the reduced density matrix is fully characterized by its Bloch vector. The time-reversal symmetry of the Ising model (1) ensures that the expectation value of the local observable  $\hat{Y}_i$  vanishes for all eigenstates. Thus, the entanglement between a single site  $i = 0$  and the rest of the infinite chain is fully determined by  $\langle \hat{Z}_0 \rangle$  and  $\langle \hat{X}_0 \rangle$  [40].

Figure 2d shows the single-site Rényi-2 entropy entanglement entropy, calculated from the  $\langle \hat{X} \rangle$  and  $\langle \hat{Z} \rangle$  data in Figs. 2a and c. The obtained entropies faithfully reproduce the predicted sharp peak at criticality and tend to zero for small  $g$ . In the ferromagnetic phase, the two symmetry-broken ground states are almost product states, featuring very little entanglement. Meanwhile,

their symmetric superposition, which is the true ground state for any finite system size, is entangled and the corresponding single-site entanglement is smooth at the critical point (dashed line).

The inset of Fig. 2d presents the nearest-neighbor concurrence (pairwise entanglement)  $C_{0,1}$  [37, 40] obtained from the measured nearest-neighbor correlators  $\hat{X}_0 \hat{X}_1$ ,  $\hat{Z}_0 \hat{Z}_1$  and  $\hat{Y}_0 \hat{Y}_1$  [41, 42]. The measured concurrence slightly deviates from theoretical predictions but aligns well with simulations of the noisy model. Notably, there is no peak in concurrence at criticality; instead, it continues to grow modestly as the system transitions into the paramagnetic phase. This suggests that the maximal single-site entanglement at criticality does not arise from strong short-distance entanglement, but rather from the accumulation of entanglement over long distances – consistent with the fact that the correlation length diverges at criticality. In contrast, in the paramagnetic phase, the nearest-neighbor entanglement dominates the nonzero single-site entanglement.

### 2. Entanglement scaling: area-law versus log-area-law

A celebrated theoretical prediction states that, for typical ground states of quantum many-body systems in  $D$  spatial dimensions, the subsystem entanglement entropy  $S(\ell)$  scales with the area of the subsystem  $\propto \ell^{D-1}$ , rather than its volume  $\propto \ell^D$  [31–33]. The predominant contributions to the entanglement entropy arise from short-range correlations around the subsystem boundary, which leads to the area-law scaling. However, the situation can change when the system becomes critical and the correlation length diverges. Specifically, for critical systems in 1D and fermionic systems with a Fermi surface of codimension  $D - 1$ , the subsystem entanglement entropy follows a log-area law  $\propto \ell^{D-1} \log \ell$  [43–48]. It has remained a considerable challenge to resolve these fundamentally different scaling laws experimentally. On the one hand, at small system sizes, it is difficult to differentiate between log-law and area-law scalings. On the other hand, when increasing the linear subsystem size  $\ell$ , it becomes more and more difficult to prepare accurate groundstate approximations, the number of measurement shots for the subsystem tomography grows, in principal, exponentially in  $\ell$ , and the rapid accumulation of noise undermines attempts to resolve the scaling behavior accurately.

However, for the 1D binary MERA, the multiscale renormalization process changes length scales by a constant factor in every renormalization step, reducing the size of a given subsystem by a factor  $1/2$ . This effectively maps a logarithmic scaling in the subsystem size  $\ell$  to a linear scaling in the number of renormalization steps  $T = 1, 2, 3, \dots$ . Consequently, distinguishing between area and log-area laws becomes a matter of checking whether the entanglement entropy saturates as a function of  $T$  or increases linearly with the renormalization

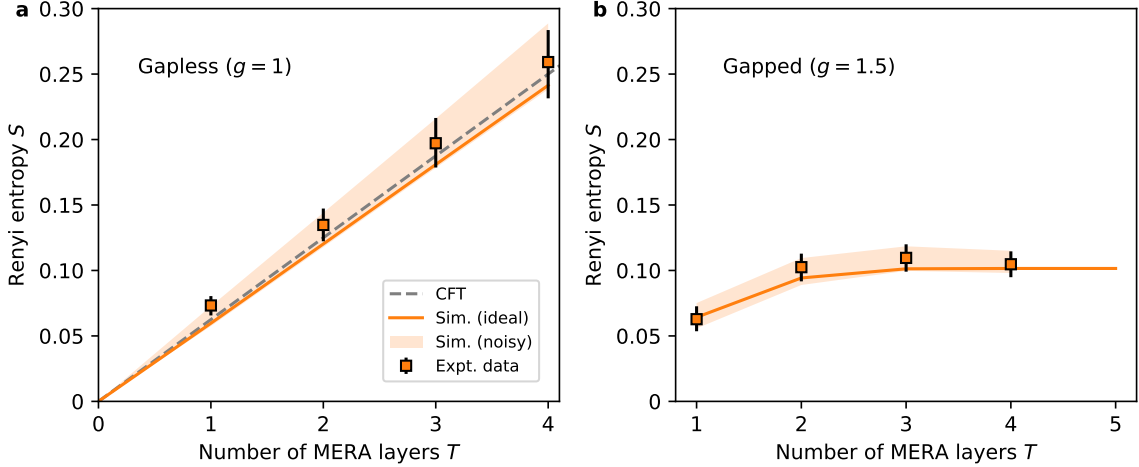


FIG. 3. **Entanglement entropy scaling for critical and gapped systems.** **a**, Log-area-law scaling of the bipartite half-chain Rényi-2 entanglement entropy for the infinite Ising chain (1) at the critical point  $g = 1$ . The finite number  $T$  of MERA layers on the  $x$ -axis corresponds to an effective system size  $N_{\text{eff}} = 3 \times 2^T$ . The gray dashed line represents the prediction of conformal field theory with a central charge  $c = 1/2$ , and the solid line corresponds to ideal MERA simulations. Both the noisy simulation (shaded area) and experimental data (dots with error bars) are shown with a 95% confidence interval based on 1,500 shots per element of the tomographic measurement basis. **b**, Area-law scaling of Rényi-2 entanglement entropy for MERA states at the non-critical point  $g = 1.5$ . Here, the half-chain entanglement saturates rapidly as the number  $T$  of MERA layers increases. Again, the solid line corresponds to ideal MERA simulations. The shaded area and error bars show 95% confidence intervals based on 8,000, 5,000, 3,000, and 2,000 shots per measurement basis element for cases with one-, two-, three-, and four-layer MERA, respectively.

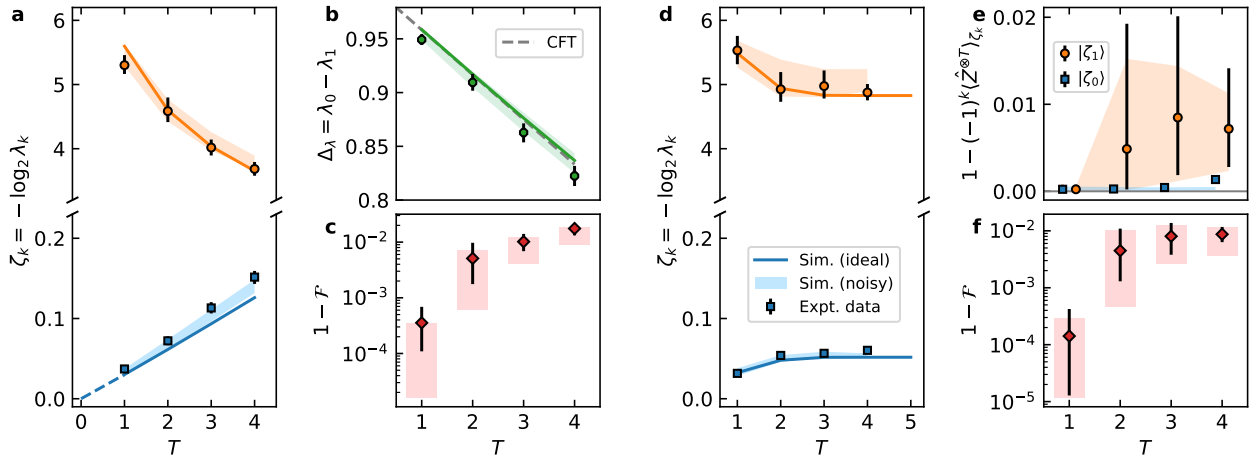


FIG. 4. **Analysis of half-chain density matrices.** **a** and **d**, Lowest eigenvalues  $\{\zeta_0, \zeta_1\}$  of the MERA entanglement Hamiltonian at the critical point  $g = 1$  and the non-critical point  $g = 1.5$ , respectively. **b**, The Schmidt gap  $\Delta_\lambda = \lambda_0 - \lambda_1$  gradually closes as the (sub)system size increases at criticality. The gray dashed line represents the theoretical approximation from Ref. [39]. **c** and **f**, Infidelity of the subsystem density matrices relative to ideal simulations at  $g = 1$  and  $g = 1.5$ , respectively. **e**, Expectation values of Pauli  $Z$ -strings for the first two eigenstates  $\{|\zeta_0\rangle, |\zeta_1\rangle\}$  of the entanglement Hamiltonian at  $g = 1.5$ . In all plots, solid lines represent ideal infinite MERA simulations. Both the noisy simulation (shaded area) and experimental data (dots) are shown with indicators for the 95% confidence intervals. The results are based on the same dataset as Fig. 3, but here, positive semi-definite density matrices are reconstructed using maximum-likelihood quantum state tomography.

step  $T$ .

In experiments, we implement formally infinite MERA with a finite number of layers  $T$ . We consider a bipartition into subsystems  $A = (-\infty, 1]$  and  $B = [2, +\infty)$  and implement the holographic subsystem tomography as described in Sec. II B and detailed in Appx. B. We prepare the MERA circuit for the causal cone of the subsystem boundary, measure the  $T$  renormalized sites at the right edge of the cone (Fig. 1), and use the classical shadow method [49] to extract the Rényi entanglement entropy (3). The finite number of MERA layers limits the maximal correlation length to  $\approx 3 \times 2^T$ . Thus, we experimentally probe effective subsystem sizes  $\ell \propto 2^T$ . See Appx. C for a more detailed argument concerning this relation of  $T$  and effective subsystem sizes.

For a non-critical point ( $g = 1.5$ ) of Ising model (1), the measured half-chain Rényi-2 entropy  $S$  as function of the number  $T$  of MERA layers is shown in Fig. 3b. We observe a rapid saturation of the entanglement entropy for  $T \geq 3$ , in agreement with the area-law. This saturation of  $S$  is expected as, due to the energy gap, the physical correlation length  $\xi$  is finite. For bond dimension  $\chi = 2$ , additional layers ( $T > 3$ ) in our simulation have negligible effect on the quality of the ground state approximation and entanglement. The lower layers already sufficiently encode the correlations of this gapped system, and, upon energy optimization, the tensors of any additional layers are very close to the identity. The low entropy values ( $S \sim 0.1$ ) imply that the state of the measured renormalized sites is close to the product state  $|0\rangle^{\otimes T}$ . In this regime, we hence expect SPAM errors and gate rotation errors due to the axial motion to be the primary error sources.

At criticality ( $g = 1$ ), the system has gapless excitations, and the physical correlation length diverges ( $\xi \rightarrow \infty$ ). Here, we model the ground state by a *scale-invariant* MERA with an infinite number of identical layers. In this case, the MERA tensors are homogeneous across both the spatial and holographic dimensions to capture the self-similar nature of the system [34]. Directly preparing a scale-invariant MERA is however impractical. Instead, we truncate the scale-invariant MERA after  $T$  layers and optimize the top layer to minimize the finite- $T$  effects as detailed in Appx. D.

The measured half-chain entanglement entropy at criticality ( $g = 1$ ) is shown as a function of the number of employed MERA layers in Fig. 3a. The observed entropy increases linearly by approximately  $1/16$  per renormalization step (MERA layer). This is consistent with the prediction  $\frac{1}{16} \log_2(\ell/a)$  of conformal field theory (dashed line), where  $a$  is an ultraviolet cutoff that regularizes the continuum field theory [50]. The slight increase in the measured  $S$  over the ideal prediction is well-described by our error model. The primary error sources here are idle dephasing and noise in gate angles due to axial motion of the ion chain (see See Appx. A).

### 3. Entanglement spectrum

Using the tomographic data of the last section, we reconstruct valid reduced density matrices  $\rho_B$  for subsystem  $B$  through maximum-likelihood quantum state tomography [51–54]. Recall, that the causal structure of MERA provides us with a compressed representation of  $\rho_B$  as a state on the  $T$  renormalized sites. This allows us to probe the entanglement spectrum [55]. Any density matrix can be expressed in the form  $\rho_B = 2^{-\sum_i \zeta_i} |\zeta_i\rangle\langle\zeta_i|$ , where  $\{\zeta_i := -\log_2 \lambda_i\}$  is the entanglement spectrum expressed in terms of the eigenvalues  $\{\lambda_i\}$  of  $\rho_B$ .

Figures 4a and d show low-lying entanglement eigenvalues  $\{\zeta_0, \zeta_1\}$  for the Ising model (1), revealing distinct behaviors at and away from the critical point. At criticality ( $g = 1$ ), the ground level  $\zeta_0$  exhibits a log-law scaling similar to that of the entanglement entropy, while the first excited level  $\zeta_1$  decreases without a clear scaling. Recall that entanglement entropy can be rewritten as  $-\log_2(\sum_i \lambda_i^2)$ , meaning that its log-area-law scaling is dominated by the scaling of the largest eigenvalue  $\lambda_0$ . As shown in Fig. 4b, the Schmidt gap  $\Delta_\lambda = \lambda_0 - \lambda_1$  gradually closes by approximately  $1/24$  per renormalization step, which agrees with the approximate theoretical scaling  $\sim \ell^{-1/24}$  found in Ref. [39], where  $\ell$  denotes again the (effective) subsystem size.

For the non-critical point  $g = 1.5$ , Fig. 4d shows that both the ground and first-excited levels saturate. Since  $g = 1.5$  lies in the  $\mathbb{Z}_2$ -symmetric paramagnetic phase, the true ground state resides in the even sector of the global spin-flip operator  $\otimes_i^N \hat{Z}_i$  and any subsystem density matrices also commute with this operator. This symmetry conservation is confirmed in the experiment by measuring the expectation values of the spin-flip operator on subsystem  $B$ . The measurement is done efficiently with the compressed representation of  $\rho_B$  on the renormalized sites, exploiting that the unitary transformation that transforms it to the actual state on  $B$  conserves the  $\mathbb{Z}_2$ -symmetry for  $g > 1$ . As observed in Fig. 4e, the associated entanglement Hamiltonian exhibits a ground state in the even sector and a first excited state in the odd  $\mathbb{Z}_2$ -symmetric sector. This behavior closely mirrors the properties of the system Hamiltonian, aligning with recent efforts to establish connections between the properties of entanglement Hamiltonians and the system Hamiltonian.

### 4. Subsystem fidelity

Finally, we compare the reconstructed density matrix  $\rho_B$  with the ideal MERA simulations and show the infidelity  $1 - \mathcal{F}$  in Figs. 4c and f for the transverse fields  $g = 1.0$  and  $1.5$ , where

$$\mathcal{F} = \left( \text{Tr} \sqrt{\sqrt{\rho_B} \rho_{\text{ideal}} \sqrt{\rho_B}} \right)^2. \quad (4)$$

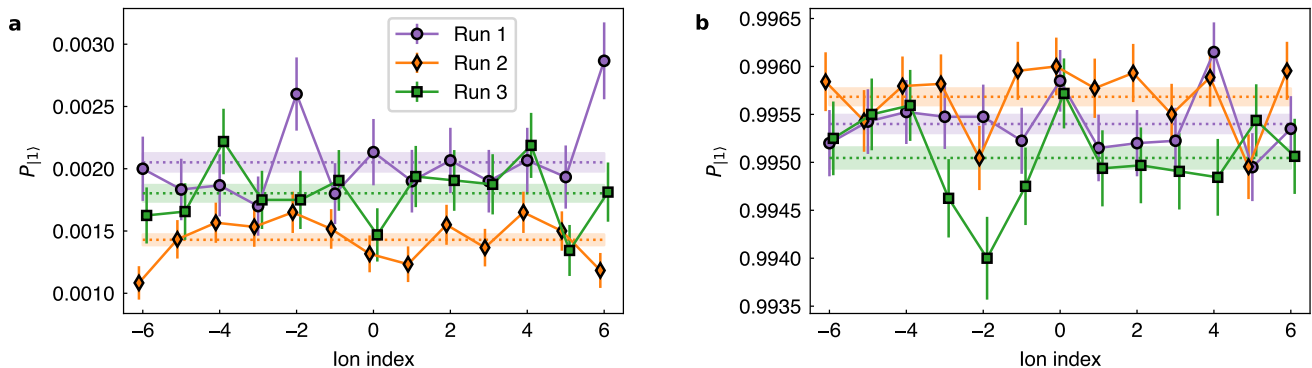


FIG. 5. State preparation and measurement (SPAM) error as a function of the ion index. **a**, Dark-state ( $|0\rangle$ ) SPAM errors, with ion-averaged values of 0.21(1)%, 0.14(0)%, and 0.18(1)% for three runs; **b**, Bright-state ( $|1\rangle$ ) SPAM errors, with ion-averaged values of 0.46(1)%, 0.43(1)%, and 0.50(1)% for three runs. Error bars and shaded areas indicate  $1\sigma$  statistical intervals.

Due to careful calibrations during the experiment, optimized ion-qubit mappings, suitable gate decompositions for the MERA circuit, and the general noise-resilience of MERA, we achieve low infidelities ranging from  $10^{-4}$  to  $10^{-2}$ . This enables the clear distinction between different entanglement scaling laws, even when the absolute difference in  $S$  is as small as  $\sim 0.15$ —a difference that could easily be obscured by experimental noise.

#### IV. CONCLUSIONS AND OUTLOOK

We used MERA on an ion-trap quantum computer to demonstrate a quantum phase transition in a condensed matter system. Furthermore, the MERA allowed us to investigate subsystem entanglement and demonstrate the transition from an area-law to a log-area-law scaling for the bipartite ground state entanglement entropy. Our experiment successfully implements the simplest MERA needed to capture the universal properties of Ising-type physics.

Extending our approach to other critical models, such as the Heisenberg model or higher-spin systems (e.g., spin-1 bilinear-biquadratic models), requires a larger MERA bond dimension  $\chi$ . This requires more qubits per renormalized site and more gates within each MERA tensor sub-circuit [24–27]. At present, we rely on classical computers to optimize the MERA and generate its corresponding quantum circuit. However, as the bond dimension increases, the classical contraction cost grows significantly, especially for higher-dimensional MERA (e.g., scaling like  $\chi^{26}$  for 2D systems). The costly classical tensor contractions can be avoided by running the MERA circuits on a quantum computer, achieving a polynomial quantum advantage [25, 26]. Achieving this requires both large numbers of qubits and high-fidelity gates with all-to-all connectivity (or efficient qubit swaps). Furthermore, techniques like qubit reset and reuse will save quantum resources since renormalized sites in MERA circuit that leave the causal cone can be measured and

reused [25, 56].

Recent advances in trapped-ion platforms have brought these requirements closer to reality. For instance, 56-qubit ion systems with 99.8% two-qubit gate fidelity are now available [57]. Larger systems, with  $\approx 128$  qubits can be made by scaling up the system used in this work. The primary error source in high-connectivity ion systems – motional heating of low-frequency modes – can be reduced by over two orders of magnitude by cryogenic techniques aided and sympathetic cooling using a different isotopic species [58]. This approach also enables qubit reset and reuse, further enhancing scalability.

#### ACKNOWLEDGMENTS

T.W. thanks K. Sun and Y. Yu for valuable discussions.

**Funding:** This work was funded by the NSF Quantum Leap Challenge Institute for Robust Quantum Simulation (OMA-2120757) and the NSF STAQ project (Phy-2325080). Support is also acknowledged from the U.S. Department of Energy, Office of Science, National Quantum Information Science Research Centers, Quantum Systems Accelerator.

**Author contributions:** Q.M. designed the MERA implementation, performed the numerical simulations, and analyzed the experimental data. T.W. ran the experiment and collected the experimental data. T.B. initiated the project and suggested the holographic subsystem tomography. M.C. supervised the experimental effort. T.B. and K.R.B. supervised the theoretical effort. All authors contributed to the manuscript.

**Competing interests:** K.R.B. is a scientific advisor for IonQ, Inc. and has a personal financial interest in the company. M.C. is a co-inventor on patents that are licensed by University of Maryland to IonQ, Inc. Other authors declare that they have no competing interests.



## Appendix A: System characterization and error model

### 1. State Preparation and Measurement Error

State preparation and measurement (SPAM) errors contribute significantly to the error budget of our MERA circuits. We determined the SPAM error for the  $|0\rangle$  state (dark)  $p_D$  by optically pumping all qubits and then performing fluorescence detection. The ion-averaged SPAM errors for the  $|0\rangle$  state, were measured as 0.21(1)%, 0.14(0)%, and 0.18(1)% across the three runs, with an inverse-variance-weighted average error of 0.16% (Fig. 5a). To measure the SPAM error for the  $|1\rangle$  state (bright)  $p_B$ , following optical pumping we applied  $R_y(\pi)$  gates to transfer all qubits to the  $|1\rangle$  state and then performed fluorescence measurement. The ion-averaged SPAM errors for the  $|1\rangle$  state were 0.46(1)%, 0.43(1)% and 0.50(1)% across the three runs, with an inverse-variance-weighted average error of 0.45% (Fig. 5b).

We calibrated the rotation angle of the  $\pi$ -pulses by applying nine consecutive  $\pi$ -gates, yielding population error  $\Delta P = 0.56_{0.12}^{0.17}\%$ , determined as the binomial proportionate 95% confidence interval using the Clopper-Pearson method. The population error resulting from single-qubit gates should scale superlinearly with number  $N_g$  of gates, corresponding to a mixture of non-correlated and correlated noise, implying population error below  $10^{-3}$  per single  $\pi$ -gate, which is below the determined bright-state SPAM error of 0.45%.

The measurement error for  $^{171}\text{Yb}^+$  hyperfine qubits arises from optical pumping between the hyperfine states during the optical detection pulse [59, 60]. We distinguish measurement from state preparation errors by varying the detection time  $t$  and fitting the count statistics and average obtained to corresponding pumping model. Extrapolating our model to the zero detection time allows us to isolate the state preparation error.

The distributions of detection counts for a single ion prepared in the bright state for different detection times are shown in Fig. 6a. Ideally, the ion would cycle between the  $|S, F=1\rangle$  and  $|P, F=0\rangle$  manifolds, resulting in a Poisson distribution of the recorded photon counts. However, the bright state can be off-resonantly pumped to the dark ground hyperfine state via the  $|S, F=1\rangle - |P, F=1\rangle$  transition detuned by 2.1 GHz, with rate  $R_b$  that is about  $5 \times 10^4$  times lower than the bright-state photon scattering rate  $\Gamma_{sc}$ . Neglecting the even slower dark-to-bright pumping process leads to the predicted distribution of the bright-state photon counts

$$P_b(n) = e^{-R_b t} \mathcal{P}(n; \varepsilon \Gamma_{sc} t) + \int_0^t \mathcal{P}(n; \varepsilon \Gamma_{sc} \tau) R_b e^{-R_b \tau} d\tau, \quad (\text{A1})$$

where  $\mathcal{P}(n; \bar{n}) = e^{-\bar{n}} \bar{n}^n / n!$  is the Poisson distribution with mean  $\bar{n}$ , and  $\varepsilon$  is the detection efficiency. The red curves in Fig. 6a show fits of the obtained count data

to this model with  $\varepsilon \Gamma_{sc} \tau$  and  $R_b$  as the fitting parameters. We average the fitted  $R_b$  values with weights inversely proportional to the fitted variances to obtain  $R_b = 3.0(1) \times 10^2 / \text{s}$ .

The detection count statistics for a single ion prepared in the dark  $|S, F=1\rangle$  state are shown in Fig. 6(f-j). The dark state can be off-resonantly pumped to the bright manifold via the 14.7-GHz detuned  $|S, F=0\rangle - |P, F=1\rangle$  transition, with rate  $R_d$  that is about  $10^6$  times lower than  $\Gamma_{sc}$ . Neglecting the reverse pumping process yields the predicted dark-state count distribution

$$P_d(n) = \int_0^t \mathcal{P}(n; \varepsilon \Gamma_{sc} (t - \tau)) e^{-R_d \tau} R_d d\tau, \quad (\text{A2})$$

A fit of this model to the count data for photon number  $n_{ph}$  above 1 in Fig. 6b yields  $R_d = 18(1) / \text{s}$ . The obtained ratio of  $R_b$  and  $R_d$  is close to the theory prediction in [61].

Preparation error  $p$  of the  $|0\rangle$  state increases the detected counts above those caused by the dark-to-bright pumping. To determine  $p$ , we fit the average detected photon number in the dark state as function of detection time in Fig. 7 to the rate equation model derived in [61]

$$\bar{n}_{ph} = \int_0^t \varepsilon \Gamma_{sc} \left( p_{d,\infty} - (p - p_{b,\infty}) e^{-(R_b + R_d)\tau} \right) d\tau \quad (\text{A3})$$

with equilibrium bright and dark state populations  $p_{b,\infty} = (R_b / R_d + 1)^{-1} = 0.056$  and  $p_{d,\infty} = 1 - (R_b / R_d + 1)^{-1} = 0.94$  and  $R_b$  and  $R_d$  determined above. The fitted value  $p = 10(6) \times 10^{-5}$  indicates that our SPAM error is dominated by the measurement error.

To model the error in state preparation, after initializing each qubit to the  $|0\rangle$  state, we randomly flip each qubit with probability  $p$ . To simulate the detection error, after running the circuit and measuring the qubits in the computational  $\{|0\rangle, |1\rangle\}$  basis, we randomly flip  $|0\rangle \rightarrow |1\rangle$  with probability  $p_D - p$  and  $|1\rangle \rightarrow |0\rangle$  with probability  $p_B - p$ .

### 2. Idling noise

We characterized the dephasing of idle qubits using a Ramsey sequence. After sequentially applying  $R_y(\frac{\pi}{2})$  gates to all 13 qubits, we simulated idling by turning off the individual-addressing Raman beams while keeping the global beam on with the same settings as during a gate sequence. After idling the qubits for a variable amount of time, we completed the Ramsey sequence by applying  $R_z(\phi)$  and  $R_y(\frac{\pi}{2})$  gates to each qubit and recording the population of the  $|1\rangle$  state as function of  $\phi$ . The fitted ion-averaged contrast  $C$  of the resulting fringes is shown as a function of the wait time  $\tau_{\text{wait}}$  on Fig. 8. A fit of the contrast data to the model  $A e^{-\tau_{\text{wait}} / T_2^*}$  yields  $T_2^* = 300(17)$  ms; the fitted  $T_2^*$  values ranged from 260 ms to 370 ms across different experiment days, with an average of 290 ms. We ascribe the measured dephasing

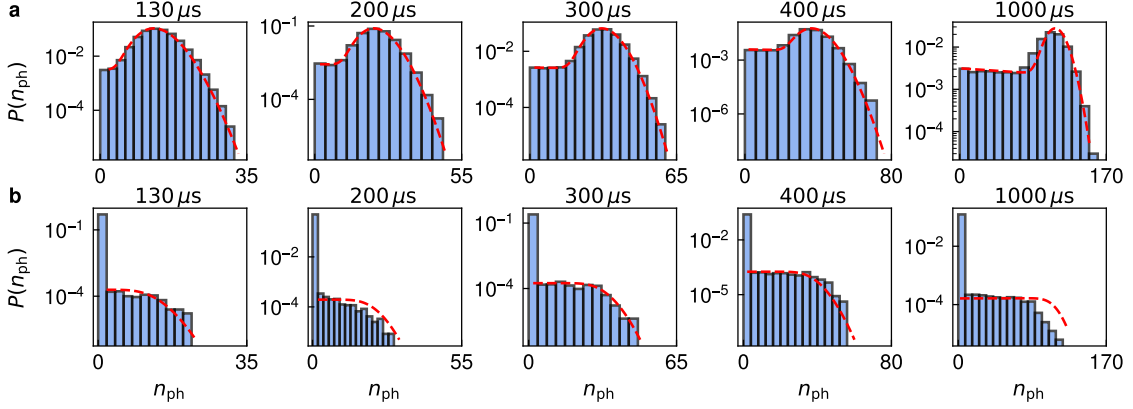


FIG. 6. Distribution of the detected photon counts  $n_{\text{ph}}$  for different detection times for the bright state (a) and the dark state (b). The red dashed lines indicate a fit to the models from Eq. (A1) and (A2).

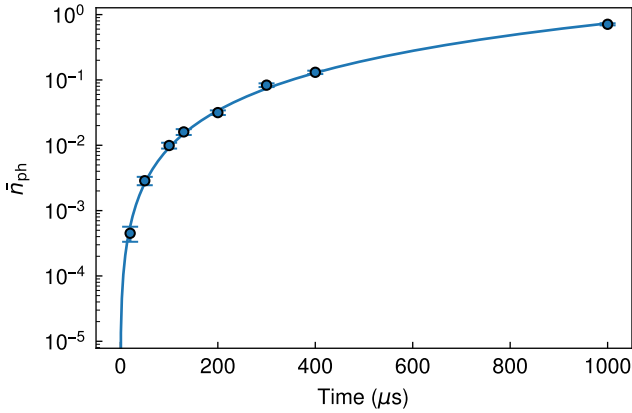


FIG. 7. The average photon number when preparing into dark state at different detection duration. The errorbars are plotted as the standard deviation of 60000 experiment shots.

to acoustic noise, chiefly from air cooling fans, in our phase-sensitive Raman interferometer setup, and expect that  $T_2^*$  times of several seconds can be obtained using phase-insensitive schemes [62] that are compatible with our experimental setup. The fitted value  $A = 0.991(1)$  reflects SPAM errors, with additional contributions potentially arising from residual single-qubit gate errors and qubit addressing and detection crosstalk.

In our simulations, we model the effects of dephasing on the qubit density matrix  $\rho$  during idling for time  $t$  via the quantum channel

$$\mathcal{E}_Z(\rho) = (1 - p_Z)\rho + p_Z Z\rho Z, \quad (\text{A4})$$

with the  $Z$ -flip probability  $p_Z = t/(2T_2^*)$ .

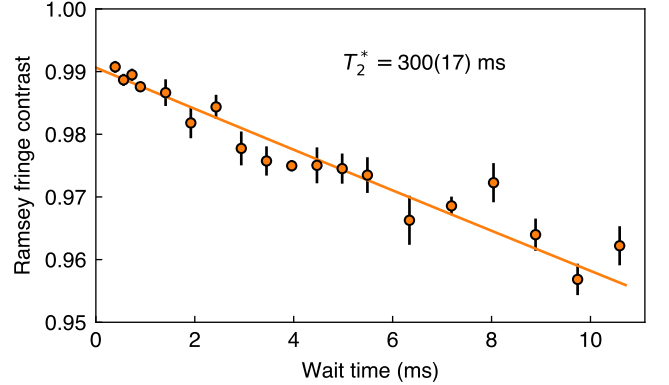


FIG. 8. The average qubit Ramsey fringe contrast as a function of the idling time  $\tau_{\text{wait}}$ . The red line represents the fit to the model  $Ae^{-\tau_{\text{wait}}/T_2^*}$  yielding  $T_2^* = 300(17) \text{ ms}$  and  $A = 0.991(1)$ . The experimental data are displayed as circular dots, with error bars indicating  $1\sigma$  fitting uncertainties.

### 3. Gate errors

#### a. Axial motion

Axial motion of our 15-ion chain, dominated by the lowest-frequency axial mode (mode 0) with frequency  $\omega_0 = 2\pi \times 241.8 \text{ kHz}$ , is an important source of errors in the experiment. This motion, which grows with time due to noisy electric fields that act on the ion chain, misaligns the ions relative to the tightly-focused addressing beams, leading to gate errors [58].

We determined the shape of the individual-addressing beams by fitting the dependence of the carrier Rabi frequency on the axial position  $x$  of a single ion to  $\Omega_0 e^{-(x-x_0)^2/w^2}$ , yielding the beam waist  $w = 646(12) \text{ nm}$ .

We quantified the addressing error after a wait time  $t$  following laser cooling by applying a variable number

$M$  of  $XX(\frac{\pi}{2})$  gates, of total duration  $\Delta t$ , to ions  $i$  and  $j$ , and measuring the resulting mean population  $p_{|11\rangle}$  of the ions in the  $|11\rangle$  state. The uncertainty in the axial motion of the ions translates into a variance in the total  $XX$  rotation angle, leading to damping of oscillations of  $p_{|11\rangle}$  with  $M$ . For  $t$  larger than several ms, this damping is governed by the statistics of the phonon number  $n_t$  of mode 0 during the applied gates [58].

We model the evolution of  $n_t$  as a biased random walk. Since the energy of mode 0 following laser cooling corresponds to hundreds of phonons, and the average heating per  $XX$  gate corresponds to more than 20 phonons, we course-grain  $n_t$  in units of  $1 \leq \delta n \ll 2n_t$  and model its random walk as

$$n_{t+\delta t} := \begin{cases} n_t + \delta n & \text{with prob. } \frac{n_t + \delta n}{\delta n} \frac{\dot{n} \delta t}{\delta n} \\ n_t - \delta n & \text{with prob. } \frac{n_t}{\delta n} \frac{\dot{n} \delta t}{\delta n} \\ n_t & \text{otherwise,} \end{cases} \quad (\text{A5})$$

where  $\dot{n}$  is the heating rate of mode 0, and the time step  $\delta t$  is chosen so that the change of  $n_t/\delta n$  remains small ( $\frac{2n_t + \delta n}{\delta n} \frac{\dot{n} \delta t}{\delta n} \leq 1$ ).

When initialized with a Boltzmann (exponential) distribution with mean  $\bar{n}_0 \gg 1$ ,  $n_t$  will remain exponentially-distributed with mean  $\bar{n}_t = \bar{n}_0 + \dot{n}t$ , where  $\dot{n}$  is the heating rate of mode 0. In this thermal limit, we find that the average phonon number  $\frac{1}{\Delta t} \int_t^{t+\Delta t} n_\tau d\tau$  between time  $t$  and  $t + \Delta t$ , has a mean of  $\mu_t = \bar{n}_{t+\Delta t/2} = \bar{n}_t + \dot{n} \frac{\Delta t}{2}$  and a variance of  $\sigma_t^2 = \mu_t^2 - \frac{\bar{n}_t \dot{n} \Delta t}{3} + \frac{\dot{n}^2 \Delta t^2}{6}$ , which can be well-approximated by a Gamma distribution with the corresponding mean and variance.

If  $M$   $XX(\theta)$  gates are applied between time  $t$  and  $t + \Delta t$ , neglecting other errors, we predict that the population of the  $|11\rangle$  state of ions  $i$  and  $j$  should be equal to

$$p_{|11\rangle}(t) = \frac{1 - C \cos(M\theta - \phi)}{2}, \quad (\text{A6})$$

with phase shift  $\phi = \alpha \arctan(\alpha M \theta \bar{\varepsilon}_{i,j}(t + \frac{\Delta t}{2}))$  and contrast  $C = (1 + [\alpha M \theta \bar{\varepsilon}_{i,j}(t + \frac{\Delta t}{2})]^2)^{-\frac{\alpha}{2}}$ , where  $\alpha = \frac{\mu_t^2}{\sigma_t^2}$ . Here,  $\bar{\varepsilon}_{i,j}(t) = \bar{\varepsilon}_i(t) + \bar{\varepsilon}_j(t)$ , where

$$\bar{\varepsilon}_i(t) = \frac{\hbar \bar{n}_t b_{i0}^2}{m \omega_0 w^2} \quad (\text{A7})$$

is the mean unitless decay parameter from [58] during the gate sequence with  $b_{i0}$  the participation rate for ion  $i$  in mode 0. In the limit of negligible heating during the  $XX$  experiment, this prediction reduces to Eq. (4) from [58].

For different ion pairs ( $i, j = -i$ ), we fit the measured mean  $|11\rangle$ -state population as function of the gate number  $M$  and the wait time  $t$  to the model from Eq. (A6). The two fitted parameters – the unitless effective decay parameter  $\bar{\varepsilon}_{i,j}(0)$  at  $t = 0$  and its rate of increase  $d\bar{\varepsilon}_{i,j}/dt$  – are shown as function of  $i$  on Fig. 9. Both fitted parameters are observed to scale with  $b_{i0}^2 + b_{j0}^2$ , indicating

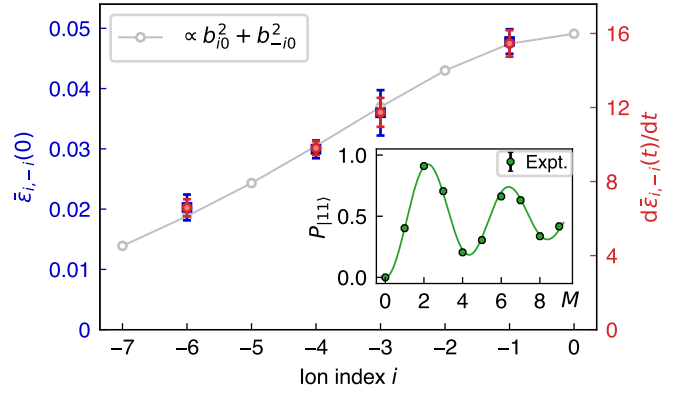


FIG. 9. The fitted initial decay parameter for  $XX$  gates between ions  $i$  and  $-i$ ,  $\bar{\varepsilon}_{i,-i}(0)$  (blue), and its rate of increase  $d\bar{\varepsilon}_{i,-i}(t)/dt$  (red). The gray line is proportional to the sum of the squares  $b_{i0}^2 + b_{-i0}^2$  of the participation factors of the addressed ions in the lowest axial mode of the ion chain. The error bars indicate  $1\sigma$  fit uncertainties. Inset shows the  $|11\rangle$ -state population of ions  $(-3, 3)$  as function of the gate number  $M$  after wait time of  $t \approx 10$  ms with fit according to Eq. (A6).

that addressing errors are dominated by motion of the lowest axial mode of the ion chain. The corresponding initial phonon number in this mode is  $\bar{n}_0 = 409(4)$  and its heating rate  $\dot{n} = 133(1)$  phonons/ms.

Using the fitted initial phonon number and heating rate above, we can model the gate rotation error for arbitrary native single- and two-qubit gates. In the noisy simulation for each shot, the initial phonon number  $n_0$  is sampled from an exponential distribution with mean  $\bar{n}_0$ . We then evolve  $n_t$  using the biased random walk model (A5) with the heating rate  $\dot{n}$ . For each rotation gate  $R(\theta)$  operating during the time interval  $[t, t + \Delta t]$  in the circuit, we compute the average phonon number  $\frac{1}{\Delta t} \int_t^{t+\Delta t} n_\tau d\tau$ . The phonon number  $n_t$  is used to determine the modeled single-qubit gate rotation angle as  $R(\theta) \rightarrow R(\theta(1 - \bar{\varepsilon}_i n_t / \bar{n}_t))$  and the two-qubit gate angle as  $X_i X_j(\theta) \rightarrow X_i X_j(\theta(1 - \bar{\varepsilon}_{i,j} n_t / \bar{n}_t))$ .

### b. $X$ -errors

We describe  $X$ -errors during entangling gates with a bit-flip channel acting on the density matrix  $\rho$  of ion  $i$  as

$$\mathcal{E}_{X,i}(\rho) = (1 - p_{X,i})\rho + p_{X,i}X_i\rho X_i, \quad (\text{A8})$$

where  $p_{X,i}$  is the  $X$ -flip probability per entangling gate.

$X$ -errors can be caused by residual spin-motion entanglement at the end of our Mølmer-Sørensen gates. These errors can be minimized by carefully choosing the motional detuning, gate duration, and envelope of our amplitude-modulated gate waveforms [63]. In-between experiment runs, we actively stabilized the frequencies of the ions' radial motional modes by performing blue-sideband Ramsey spectroscopy. Each of the middle 11 qubits was used to query one of the 11 modes from the

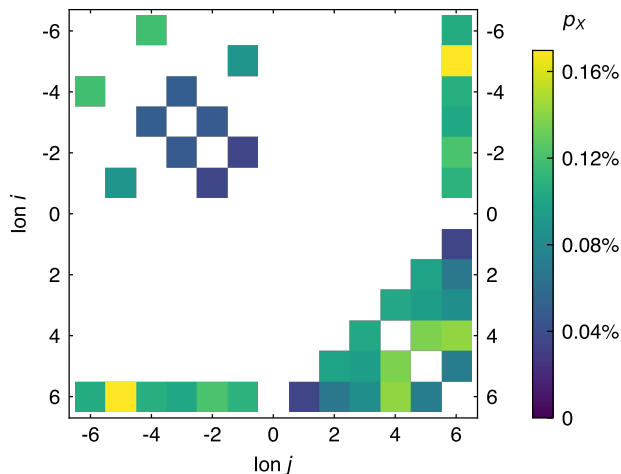


FIG. 10. Pauli  $X$  error per fully-entangling  $XX$  gate between ions  $i$  and  $j$ . Error data are shown only for gate pairs utilized in this work.

lower-frequency radial mode set that are addressed by the entangling gate waveforms. The obtained spectroscopical data was used to automatically adjust the quadratic and quartic terms in the static axial potential of the trap, as well as a common offset frequency for all gates.

We measured the probability of  $X$ -flip errors by tracking the parity  $P_{ij}(M)$  of ions  $i$  and  $j$  after applying  $M$  consecutive  $XX(\frac{\pi}{2})$  gates on this ion pair. We distinguished  $X$ -flip errors from coherent  $XX$  gate crosstalk by focusing on the shots where only the target qubits are flipped. We calculate the  $X$ -flip error probability on ion  $i$ ,  $p_{X,i}$ , as  $(1 - P_{ij}(M))/M/2$ .

### c. $Z$ -errors

To measure the Stark shifts during the entangling gates, we insert  $N_g$  pairs of  $XX(\frac{\pi}{2}) - XX(-\frac{\pi}{2})$  gates into a Ramsey sequence consisting of  $R_y(\frac{\pi}{2})$  initial and  $R_z(\phi) - R_y(\frac{\pi}{2})$  final pulses on each pair of target ions. After adjusting the qubit frequencies during each gate to compensate for the measured shifts, we use the same experimental sequence to estimate the residual gate errors.

The fitted contrast of the resulting Ramsey fringes for a sample gate is shown on Fig. 11a. The dependence of the fitted contrast on  $N_g$  is roughly quadratic, indicating that, in each shot, the phase shift error accumulates coherently as the number of gates increases. Since our Ramsey sequence puts the qubits into the  $X$ -basis, we expect gate  $X$ -errors to not affect the measured contrast. We also verified that adding a  $XX(\theta)$  gate before the  $R_z$  gates does not improve the measured contrast.

We model the observed decoherence as arising from correlated fluctuations in the gate-induced Stark shift. Such noise can arise from fluctuations in the balance of the amplitudes of the red and blue tones of the Moelmer-Soerensen gate resulting from air turbulence in the Ra-

man beam setup.

We assume that the induced phase shift  $\phi_i$  on ion  $i$  per one fully-entangling  $XX$  gate follows Gaussian distribution with mean zero and standard deviation  $\sigma_\phi^i$ , resulting in fringe contrast proportional to  $e^{-(N_g \sigma_\phi^i)^2/2}$ . Fits of this model to the contrast data are shown in Fig. 11a as the solid lines. The fitted values of  $\sigma_\phi^i$  for fully-entangling gates on all ion pairs  $(i, j)$  used in this work are shown in Fig. 11b.

In noisy simulation for each shot, we sample a random number  $s$  from the Gaussian distribution  $\mathcal{N}(0, 1)$ . During running the circuit, we replace the ideal  $XX(\theta)$  gate on ions  $i$  and  $j$  by

$$e^{-\frac{i}{2}(\theta \hat{X}_i \hat{X}_j + \phi_i \hat{Z}_i + \phi_j \hat{Z}_j)}, \quad (\text{A9})$$

where  $\phi_i = s \frac{\sigma_\phi^i |\theta|}{\pi/2}$  is a rescaled phase shift on ion  $i$ .

## Appendix B: Holographic subsystem tomography and entanglement scaling

For the study of bipartite entanglement entropies, entanglement spectra, and subsystem fidelity as discussed in Sec. III, we consider MERA approximations  $|\Psi\rangle$  for the ground state with a bipartition into subsystem  $A$  and its complement  $B$ . The goal of the holographic subsystem tomography is to efficiently access the reduced density matrix  $\rho_B = \text{Tr}_A |\Psi\rangle\langle\Psi|$  of subsystem  $B$  in the experiment. The isometric property ( $\hat{U}^\dagger \hat{U} = \mathbb{1}$ ) of the MERA tensors implies that, under the partial trace  $\text{Tr}_A$ , all tensors outside the causal cone of  $B$  can be removed as indicated by the shaded area atop subsystem  $A$  in Fig. 12. Furthermore, all studied quantities are invariant under unitary transformation on subsystem  $B$ . We use this invariance, to apply the unitary transformation  $\hat{W}_B$  which removes all MERA tensors outside the causal cone of subsystem  $A$  as indicated by the shaded area atop subsystem  $B$  in Fig. 12.

What remains are only the tensors inside the causal cone of the boundary/boundaries between the subsystems. All qubits outside of the causal cone are in the reference state  $|0\rangle$  and need not be realized in the experiment. To determine the unitarily transformed subsystem density matrix

$$\hat{W}_B^\dagger \rho_B \hat{W}_B = \text{Tr}_A (\hat{W}_B^\dagger |\Psi\rangle\langle\Psi| \hat{W}_B) \quad (\text{B1})$$

we only need to implement the MERA circuits for the causal-cone of the subsystem interface and measure the non-trivial renormalized sites at the boundary of  $B$ . These are indicated by diamonds in Fig. 12.

To lower experimental resource requirements further, we either consider infinite chains with a bipartition into two semi-infinite subsystems, or systems with periodic boundary conditions where block  $B$  is large enough such that the causal cones of its two edges are disjoint as exemplified in Fig. 12. In this scenario, the transformed

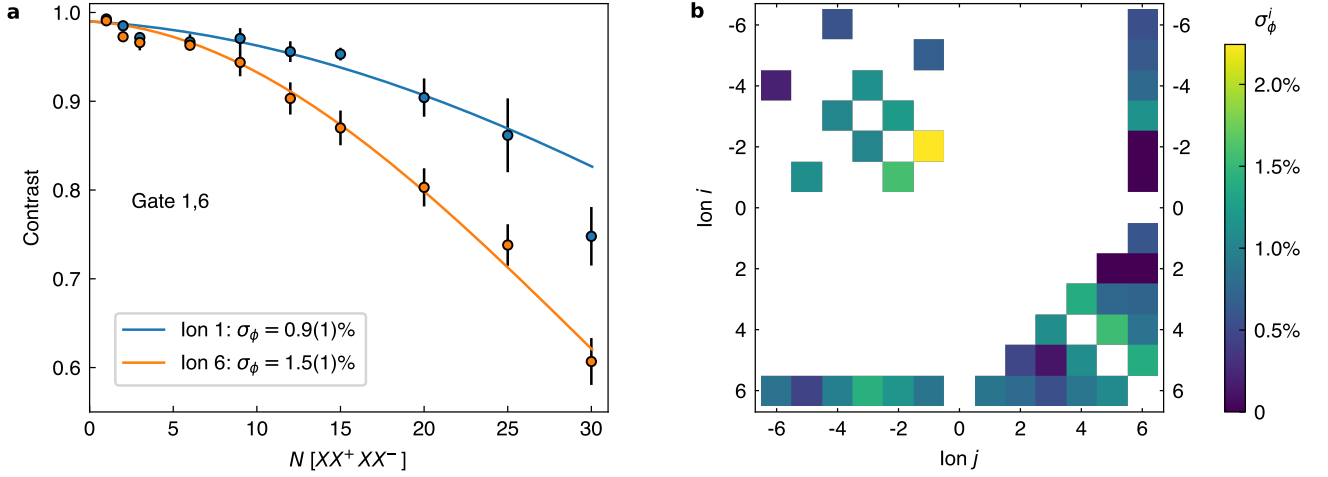


FIG. 11. **a**, Ramsey fringe contrast as a function of the number of  $(XX^+, XX^-)$  gate pairs inside the Ramsey sequence for a sample gate. **b**, Standard deviation  $\sigma_\phi^i$  of the fitted random phase shift  $\phi_i$  on ion  $i$  per fully-entangling  $XX$  gate on ion pair  $(i, j)$ . Error data are shown only for gate pairs utilized in this work.

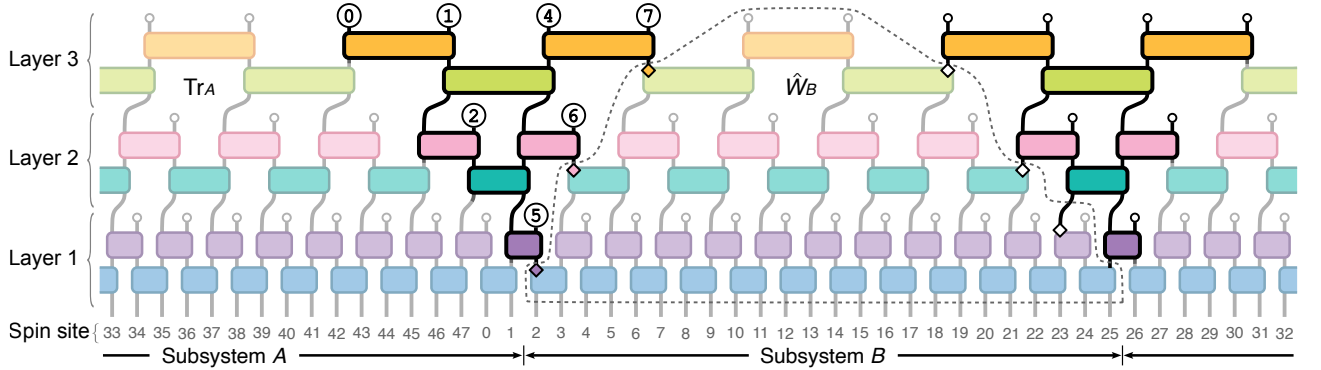


FIG. 12. Holographic subsystem tomography and entanglement scaling. An infinite binary MERA with  $T$  layers is consistent with a MERA for a system of  $N = 6 \times 2^T$  sites with periodic boundary conditions. Here,  $T = 3$  and hence  $N = 6 \times 2^3 = 48$ . All connected two-point correlation functions for sites of distance  $\geq 3 \times 2^T - 2 = 22$  are exactly zero. For example,  $\langle \hat{X}_{10} \hat{Y}_{31} \rangle - \langle \hat{X}_{10} \rangle \langle \hat{Y}_{31} \rangle$  can be nonzero while  $\langle \hat{X}_{10} \hat{Y}_{32} \rangle - \langle \hat{X}_{10} \rangle \langle \hat{Y}_{32} \rangle \equiv 0$ . This is due to the fact that, in the latter case, the causal cones of two operators have no overlap. Similarly, for any bipartition of the system into equally sized blocks like  $A = \{26, \dots, 47, 0, 1\}$  and  $B = \{2, \dots, 25\}$ , the causal cones of the two subsystem boundaries do not overlap. Hence, measurements of the renormalized sites at the two boundaries are independent of each other, i.e., follow a product distribution.

density operator (B1) is actually a tensor product of a state  $\rho_B^L$  at the left edge, a state  $\rho_B^R$  at the right edge, and central sites in the reference state  $|0\rangle$ . It is then sufficient to measure only at the left edge, as  $\rho_B^R$  is identical (up to a spatial reflection). Hence, in this holographic tomography scheme, we only need to measure the state of  $T$  renormalized sites, where  $T$  is the number of MERA layers.

### Appendix C: Subsystem size versus number of MERA layers

In the main text, we associated the number  $T$  of MERA layers with the logarithm of subsystem sizes  $\ell$ . Let us explain the relation in more detail here.

The infinite, binary 1D MERA  $|\Psi\rangle$  with  $T$  layers has a maximal correlation range  $\xi_{\max} = 3 \times 2^T$ , where the prefactor 3 arises from the maximal causal-cone width of local operators that act non-trivially on  $k \leq 3$  contiguous sites. In particular, connected correlation functions

$$\langle \hat{O}_i \hat{O}'_{i+\delta\ell} \rangle_\Psi - \langle \hat{O}_i \rangle \langle \hat{O}'_{i+\delta\ell} \rangle = 0 \quad (\text{C1})$$

are exactly zero for all  $i$  and local operators  $\hat{O}_i$  and  $\hat{O}'_j$  whenever  $\delta\ell \geq \xi_{\max} - 3 + k$ .

As a result, all local observables, two-point correlation functions, and subsystem density matrices  $\rho_B$  for blocks of  $\ell \leq \xi_{\max}$  sites of an infinite MERA with  $T$  layers agree with those of a corresponding finite-size MERA for a system of  $L = 6 \times 2^T$  sites with periodic boundary conditions.

In conclusion, the effective half-chain density opera-

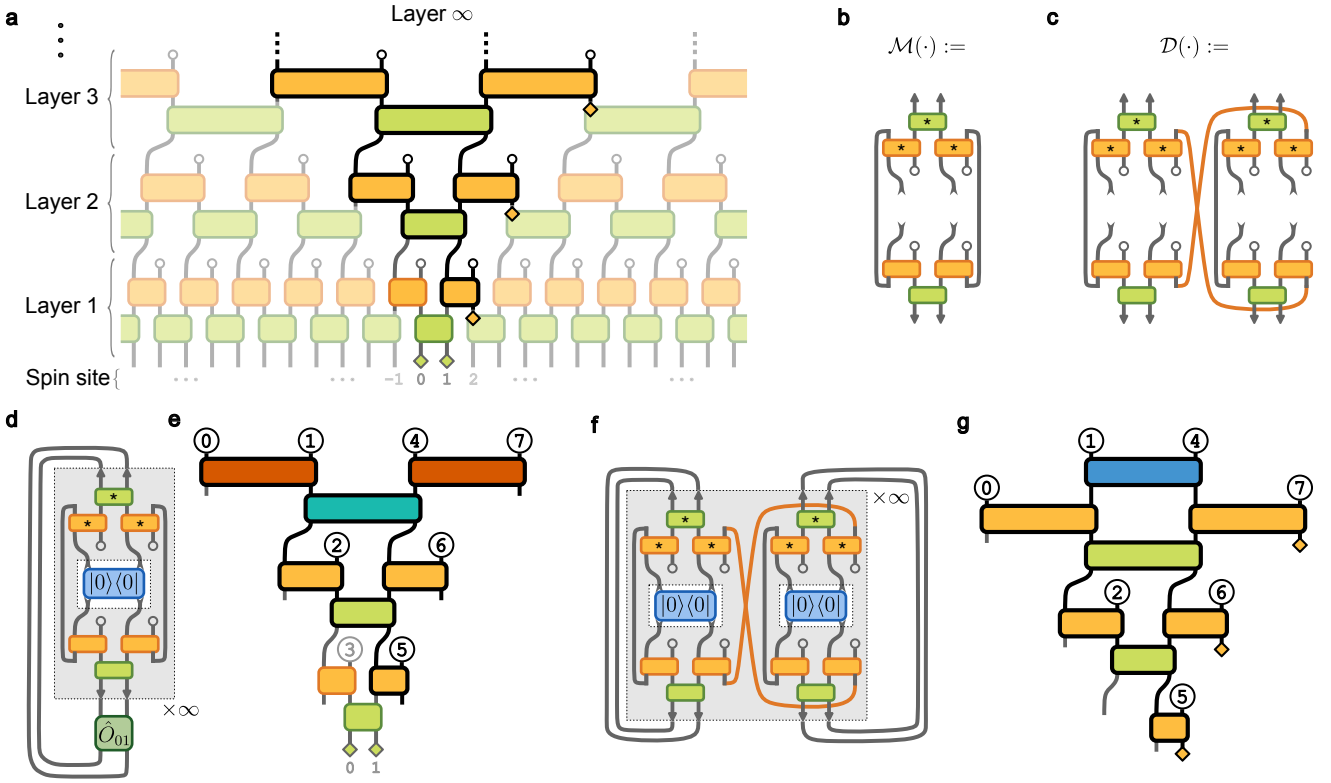


FIG. 13. Scale-invariant MERA and its implementation on a quantum computer. **a**, A scale-invariant binary 1D MERA with infinite lattice sites in the physical dimension and infinite number of layers in the holographic dimension. All unitaries (light-green boxes without open circles) and isometries (orange boxes with open circles) are identical across layers and the spatial direction. **b**, Local observables on sites 0 and 1 have a causal cone consisting of a repeating set of tensors in each layer. The corresponding repeated layer transition map  $\mathcal{M}(\cdot)$  maps reduced density matrices from the top to the bottom layer. Stars indicate complex conjugation. **c**, A doubled and SWAP-contracted channel  $\mathcal{D}$  for calculating the second-order Rényi entanglement entropy of a bipartition into subsystems  $(-\infty, 1]$  and  $[2, \infty)$  (see panel **f**). **d**, Causal-cone tensor-network for the evaluation of local expectation values on sites 0 and 1. Without loss of generality, the MERA circuit is initialized with reference state  $|0\rangle$  at the top layer. **e**, In the experiment, we truncate the scale-invariant MERA at  $T$  layers. For the measurement of local observables, the top layer is optimized to approximate the dominant eigenmode  $\rho_0 := \lim_{n \rightarrow \infty} \mathcal{M}^n(|0\rangle\langle 0|)$  of the layer transition map. Finally, we measure the qubits at sites 0 and 1. **f**, The tensor network for the purity of the reduced density operator of subsystem  $[2, \infty)$ . **g**, In this case, the top layer is optimized to suppress sub-leading contributions from the eigenvectors of the doubled channel  $\mathcal{D}$ . Scale-invariant layers are then appended. To extract the scaling of entanglement across  $T$  different energy scales, we perform tomography on  $T$  qubits at the right edge of the boundary causal-cone circuit.

tors (B1) of infinite  $T$ -layer MERA considered in Sec. III agree with those of  $\ell = 3 \times 2^T$  site blocks of a periodic system with a total of  $6 \times 2^T$  sites, establishing the exponential relation between  $\ell$  and  $T$ .

#### Appendix D: Scale-invariant MERA

Scale-invariant MERA is a tensor network designed for critical systems with diverging correlation lengths. As shown in Fig. 13a, it features a repeating structure across layers, with identical tensors representing different length scales, allowing it to efficiently capture the self-similarity and entanglement scaling of infinite systems.

Viewed in the renormalization direction, the scale-invariant MERA coarse-grains the local Hamiltonian of a critical system into an RG fixed point. Seen in reverse,

the scale-invariant MERA acts as a quantum channel that iteratively refines the state, starting from an initial reference state and adding layers to construct the ground state of the critical system.

Consider the spin sites 0 and 1. Their causal-cone state (unshaded region in Fig. 13a) is constructed by iteratively applying the same layer-transition map  $\mathcal{M}$  (Fig. 13b) layer by layer to the input states. This layer-transition map is a valid quantum channel, which can be diagonalized in bi-orthonormal bases  $\mathcal{M}(\cdot) = |\hat{\rho}_{\text{steady}}\rangle\rangle\langle\langle \mathbb{1} | + \sum_{i>0} \lambda_i |\hat{r}_i\rangle\rangle\langle\langle \hat{\ell}_i |$ , with  $\lambda_i < 1$  for all  $i > 0$ . Without loss of generality, we assume the MERA circuit is initialized in a zero product state  $|0\rangle$  at the topmost (infinite) layer. The expectation value of a local observable  $\hat{O}_{01}$  with the scale-invariant MERA is then given by

$$\lim_{n \rightarrow \infty} \text{Tr} \left( \hat{O}_{01} \mathcal{M}^n(|0\rangle\langle 0|) \right) = \text{Tr} \left( \hat{O}_{01} \hat{\rho}_{\text{steady}} \right), \quad (\text{D1})$$

as shown in Fig. 13d. In the experiment, we can not directly prepare a MERA circuit with infinite layers. Instead, at the  $T$ -th layer, we first prepare a two-site state  $\hat{\rho}'$  that maximizes the contribution of the dominant eigenmode  $\hat{\rho}_{\text{steady}}$ . This is achieved by determining the gate angles  $\{\theta\}$  in the  $T$ -th layer w.r.t.  $\arg \min_{\theta} \sum_{i>0} |\langle \hat{\ell}_i | \hat{\rho}' \rangle|^2$ . We then append  $T - 1$  scale-invariant layers to further refine the dominant eigenmode, as shown in Fig. 13e. This approach is highly effective in practice, as demonstrated with  $T = 5$  for local observables discussed in Sec. III A and Sec. III B 1.

Now, we introduce a doubled and SWAP-contracted channel  $\mathcal{D}(\cdot) = \sum_i \Lambda_i |R_i\rangle\langle L_i|$ , with  $|\Lambda_0| > |\Lambda_i|$  for all  $i > 1$ , as shown in Fig. 13c. The purity of subsystem  $B$  can be computed by iteratively applying  $\mathcal{D}$  to the zero product state  $|\mathbf{0}\rangle\langle\mathbf{0}|$  at the topmost  $n$ -th layer and taking the final trace as  $\text{Tr}(\mathcal{D}^n(|\mathbf{0}\rangle\langle\mathbf{0}|))$ , see Fig. 13f. The corresponding second-order Rényi entropy for a scale-invariant

MERA with infinite layers is given by

$$\begin{aligned} S &= -\lim_{n \rightarrow \infty} \log_2(\text{Tr}(\mathcal{D}^n(|\mathbf{0}\rangle\langle\mathbf{0}|))) \\ &= -\log_2\left(\lim_{n \rightarrow \infty} \sum_{i=0} \Lambda_i^n \langle \mathbb{1} | R_i \rangle \langle L_i | \mathbf{0} \rangle\right) \\ &= -n \log_2 \Lambda_0 - \log_2(\langle \mathbb{1} | R_0 \rangle \langle L_0 | \mathbf{0} \rangle). \end{aligned} \quad (\text{D2})$$

The last line consists of a linear scaling with the total number of layers  $n$  and a constant offset. This indicates that for a deep MERA ( $n \gg 1$ ) with open boundary conditions, the half-chain entanglement entropy follows a log-law, with sub-leading corrections due to boundary effects, as the total system size  $\propto 2^n$  increases. Alternatively, for a scale-invariant MERA with infinite spatial size, the half-chain entanglement entropy obeys the logarithmic law as the energy scale changes by adding renormalization step.

Again, we cannot directly implement an infinite-layer MERA in the experiment. Instead, we first prepare a two-site state  $\hat{\rho}'$  by applying a two-qubit tensor with parameters  $\{\theta\}$  to suppress subleading contributions from the channel  $\mathcal{D}$ . Formally, we choose  $\{\theta\}$  to minimize  $\sum_{i>0} |\langle \mathbb{1} | R_i \rangle \langle L_i | \hat{\rho}' \rangle|^2$ . We then append  $T$  scale-invariant layers, yielding

$$S = -\log_2(\text{Tr}(\mathcal{D}^T(\hat{\rho}'))) \approx -T \log_2 \Lambda_0. \quad (\text{D3})$$

Finally, we perform subsystem state tomography on all  $T$  qubits at the right edge of the boundary causal-cone state. Fig. 13g gives an example of the corresponding quantum circuit one can implement in experiment, and we use  $T = 4$  in Sec. III B 2 and III B 3.

- 
- [1] S. L. Sondhi, S. M. Girvin, J. P. Carini, and D. Shahar, Continuous quantum phase transitions, *Rev. Mod. Phys.* **69**, 315 (1997).
- [2] S. Sachdev, *Quantum Phase Transitions*, 2nd ed. (Cambridge University Press, Cambridge, UK, 2011).
- [3] I. Bloch, J. Dalibard, and W. Zwerger, Many-body physics with ultracold gases, *Rev. Mod. Phys.* **80**, 885 (2008).
- [4] A. Smith, M. Kim, F. Pollmann, and J. Knolle, Simulating quantum many-body dynamics on a current digital quantum computer, *npj Quantum Information* **5**, 106 (2019).
- [5] F. Barratt, J. Dborin, M. Bal, V. Stojevic, F. Pollmann, and A. G. Green, Parallel quantum simulation of large systems on small nisq computers, *npj Quantum Information* **7**, 79 (2021).
- [6] M. Meth, V. Kuzmin, R. van Bijnen, L. Postler, R. Stricker, R. Blatt, M. Ringbauer, T. Monz, P. Silvi, and P. Schindler, Probing phases of quantum matter with an ion-trap tensor-network quantum eigensolver, *Phys. Rev. X* **12**, 041035 (2022).
- [7] J. Dborin, V. Wimalaweera, F. Barratt, E. Ostby, T. E. O'Brien, and A. G. Green, Simulating groundstate and dynamical quantum phase transitions on a superconducting quantum computer, *Nature Communications* **13**, 5977 (2022).
- [8] Q. Zhu, Z.-H. Sun, M. Gong, F. Chen, Y.-R. Zhang, Y. Wu, Y. Ye, C. Zha, S. Li, S. Guo, H. Qian, H.-L. Huang, J. Yu, H. Deng, H. Rong, J. Lin, Y. Xu, L. Sun, C. Guo, N. Li, F. Liang, C.-Z. Peng, H. Fan, X. Zhu, and J.-W. Pan, Observation of thermalization and information scrambling in a superconducting quantum processor, *Phys. Rev. Lett.* **128**, 160502 (2022).
- [9] M. Tajik, M. Gluza, N. Sebe, P. Schüttelkopf, F. Cataldini, J. Sabino, F. Møller, S.-C. Ji, S. Erne, G. Guarnieri, S. Sotiriadis, J. Eisert, and J. Schmiedmayer, Experimental observation of curved light-cones in a quantum field simulator, *Proceedings of the National Academy of Sciences* **120**, e2301287120 (2023).
- [10] F. Fang, K. Wang, V. S. Liu, Y. Wang, R. Cimmino, J. Wei, M. Bintz, A. Parr, J. Kemp, K.-K. Ni, and N. Y. Yao, *Probing critical phenomena in open quantum systems using atom arrays* (2024), arXiv:2402.15376 [quant-ph].
- [11] R. Islam, R. Ma, P. M. Preiss, M. Eric Tai, A. Lukin, M. Rispoli, and M. Greiner, Measuring entanglement en-

- trophy in a quantum many-body system, *Nature* **528**, 77–83 (2015).
- [12] K. Li, M. Han, D. Qu, Z. Huang, G. Long, Y. Wan, D. Lu, B. Zeng, and R. Laflamme, Measuring holographic entanglement entropy on a quantum simulator, *npj Quantum Information* **5**, 30 (2019).
- [13] A. Bergschneider, V. M. Klinkhamer, J. H. Becher, R. Klemt, L. Palm, G. Zürn, S. Jochim, and P. M. Preiss, Experimental characterization of two-particle entanglement through position and momentum correlations, *Nature Physics* **15**, 640 (2019).
- [14] T. Brydges, A. Elben, P. Jurcevic, B. Vermersch, C. Maier, B. P. Lanyon, P. Zoller, R. Blatt, and C. F. Roos, Probing rényi entanglement entropy via randomized measurements, *Science* **364**, 260 (2019).
- [15] M. Foss-Feig, S. Ragole, A. Potter, J. Dreiling, C. Figgatt, J. Gaebler, A. Hall, S. Moses, J. Pino, B. Spaun, B. Neyenhuis, and D. Hayes, Entanglement from tensor networks on a trapped-ion quantum computer, *Phys. Rev. Lett.* **128**, 150504 (2022).
- [16] M. Tajik, I. Kukuljan, S. Sotiriadis, B. Rauer, T. Schweigler, F. Cataldini, J. Sabino, F. Møller, P. Schüttelkopf, S.-C. Ji, *et al.*, Verification of the area law of mutual information in a quantum field simulator, *Nature Physics* **19**, 1022 (2023).
- [17] M. K. Joshi, C. Kokail, R. van Bijnen, F. Kranzl, T. V. Zache, R. Blatt, C. F. Roos, and P. Zoller, Exploring large-scale entanglement in quantum simulation, *Nature* **624**, 539 (2023).
- [18] A. H. Karamlou, I. T. Rosen, S. E. Muschinske, C. N. Barrett, A. Di Paolo, L. Ding, P. M. Harrington, M. Hays, R. Das, D. K. Kim, *et al.*, Probing entanglement in a 2d hard-core bose–hubbard lattice, *Nature* **629**, 561 (2024).
- [19] T. Barthel and J. Lu, Fundamental limitations for measurements in quantum many-body systems, *Phys. Rev. Lett.* **121**, 080406 (2018).
- [20] J. R. McClean, S. Boixo, V. N. Smelyanskiy, R. Babush, and H. Neven, Barren plateaus in quantum neural network training landscapes, *Nature Communications* **9**, 10.1038/s41467-018-07090-4 (2018).
- [21] M. Cerezo, A. Sone, T. Volkoff, L. Cincio, and P. J. Coles, Cost function dependent barren plateaus in shallow parametrized quantum circuits, *Nature Communications* **12**, 10.1038/s41467-021-21728-w (2021).
- [22] G. Vidal, Entanglement renormalization, *Phys. Rev. Lett.* **99**, 220405 (2007).
- [23] G. Vidal, Class of quantum many-body states that can be efficiently simulated, *Phys. Rev. Lett.* **101**, 110501 (2008).
- [24] R. Haghshenas, J. Gray, A. C. Potter, and G. K.-L. Chan, Variational power of quantum circuit tensor networks, *Phys. Rev. X* **12**, 011047 (2022).
- [25] Q. Miao and T. Barthel, Quantum-classical eigensolver using multiscale entanglement renormalization, *Phys. Rev. Res.* **5**, 033141 (2023).
- [26] Q. Miao and T. Barthel, Convergence and quantum advantage of trotterized mera for strongly-correlated systems (2023), [arXiv:2303.08910 \[quant-ph\]](https://arxiv.org/abs/2303.08910).
- [27] R. Haghshenas, E. Chertkov, M. DeCross, T. M. Gatterman, J. A. Gerber, K. Gilmore, D. Gresh, N. Hewitt, C. V. Horst, M. Matheny, T. Mengle, B. Neyenhuis, D. Hayes, and M. Foss-Feig, Probing critical states of matter on a digital quantum computer (2023), [arXiv:2305.01650 \[quant-ph\]](https://arxiv.org/abs/2305.01650).
- [28] I. H. Kim and B. Swingle, Robust entanglement renormalization on a noisy quantum computer, [arXiv:1711.07500](https://arxiv.org/abs/1711.07500) (2017).
- [29] T. Barthel and Q. Miao, Absence of barren plateaus and scaling of gradients in the energy optimization of isometric tensor network states, [arXiv:2304.00161](https://arxiv.org/abs/2304.00161) (2023).
- [30] Q. Miao and T. Barthel, Isometric tensor network optimization for extensive hamiltonians is free of barren plateaus, *Phys. Rev. A* **109**, L050402 (2024).
- [31] J. Eisert, M. Cramer, and M. B. Plenio, Colloquium: Area laws for the entanglement entropy, *Rev. Mod. Phys.* **82**, 277 (2010).
- [32] J. I. Latorre and A. Riera, A short review on entanglement in quantum spin systems, *J. Phys. A: Math. Theor.* **42**, 504002 (2009).
- [33] N. Laflorencie, Quantum entanglement in condensed matter systems, *Phys. Rep.* **646**, 1 (2016).
- [34] S. Montangero, M. Rizzi, V. Giovannetti, and R. Fazio, Critical exponents with a multiscale entanglement renormalization ansatz channel, *Phys. Rev. B* **80**, 113103 (2009).
- [35] P. L. W. Maunz, High optical access trap 2.0., *osti.gov*, SAND2016 (2016).
- [36] P. Pfeuty, The one-dimensional ising model with a transverse field, *Annals of Physics* **57**, 79 (1970).
- [37] T. J. Osborne and M. A. Nielsen, Entanglement in a simple quantum phase transition, *Phys. Rev. A* **66**, 032110 (2002).
- [38] H. A. Kramers and G. H. Wannier, Statistics of the two-dimensional ferromagnet. part i, *Phys. Rev.* **60**, 252 (1941).
- [39] G. De Chiara, L. Lepori, M. Lewenstein, and A. Sanpera, Entanglement spectrum, critical exponents, and order parameters in quantum spin chains, *Phys. Rev. Lett.* **109**, 237208 (2012).
- [40] A. Osterloh, L. Amico, G. Falci, and R. Fazio, Scaling of entanglement close to a quantum phase transition, *Nature* **416**, 608 (2002).
- [41] O. F. Syljuåsen, Entanglement and spontaneous symmetry breaking in quantum spin models, *Phys. Rev. A* **68**, 060301 (2003).
- [42] T. R. de Oliveira, G. Rigolin, M. C. de Oliveira, and E. Miranda, Symmetry-breaking effects upon bipartite and multipartite entanglement in the  $xy$  model, *Phys. Rev. A* **77**, 032325 (2008).
- [43] M. Srednicki, Entropy and area, *Phys. Rev. Lett.* **71**, 666 (1993).
- [44] C. Callan and F. Wilczek, On geometric entropy, *Phys. Lett. B* **333**, 55 (1994).
- [45] C. Holzhey, F. Larsen, and F. Wilczek, Geometric and renormalized entropy in conformal field theory, *Nucl. Phys. B* **424**, 443 (1994).
- [46] M. M. Wolf, Violation of the entropic area law for fermions, *Phys. Rev. Lett.* **96**, 010404 (2006).
- [47] D. Gioev and I. Klich, Entanglement entropy of fermions in any dimension and the Widom conjecture, *Phys. Rev. Lett.* **96**, 100503 (2006).
- [48] T. Barthel, M.-C. Chung, and U. Schollwöck, Entanglement scaling in critical two-dimensional fermionic and bosonic systems, *Phys. Rev. A* **74**, 022329 (2006).
- [49] H.-Y. Huang, R. Kueng, and J. Preskill, Predicting many properties of a quantum system from very few measurements, *Nature Physics* **16**, 1050 (2020).



- [50] P. Calabrese and J. Cardy, Entanglement entropy and conformal field theory, *Journal of Physics A: Mathematical and Theoretical* **42**, 504005 (2009).
- [51] Z. Hradil, Quantum-state estimation, *Phys. Rev. A* **55**, R1561 (1997).
- [52] J. Řeháček, Z. Hradil, and M. Ježek, Iterative algorithm for reconstruction of entangled states, *Phys. Rev. A* **63**, 040303 (2001).
- [53] J. Fiurášek, Maximum-likelihood estimation of quantum measurement, *Phys. Rev. A* **64**, 024102 (2001).
- [54] D. F. V. James, P. G. Kwiat, W. J. Munro, and A. G. White, Measurement of qubits, *Phys. Rev. A* **64**, 052312 (2001).
- [55] H. Li and F. D. M. Haldane, Entanglement spectrum as a generalization of entanglement entropy: Identification of topological order in non-abelian fractional quantum hall effect states, *Phys. Rev. Lett.* **101**, 010504 (2008).
- [56] M. DeCross, E. Chertkov, M. Kohagen, and M. Foss-Feig, Qubit-reuse compilation with mid-circuit measurement and reset, *Phys. Rev. X* **13**, 041057 (2023).
- [57] M. DeCross, R. Haghshenas, M. Liu, E. Rinaldi, J. Gray, Y. Alexeev, C. H. Baldwin, J. P. Bartolotta, M. Bohn, E. Chertkov, J. Cline, J. Colina, D. DelVento, J. M. Dreiling, C. Foltz, J. P. Gaebler, T. M. Gatterman, C. N. Gilbreth, J. Giles, D. Gresh, A. Hall, A. Hankin, A. Hansen, N. Hewitt, I. Hoffman, C. Holliman, R. B. Hutson, T. Jacobs, J. Johansen, P. J. Lee, E. Lehman, D. Lucchetti, D. Lykov, I. S. Madjarov, B. Mathewson, K. Mayer, M. Mills, P. Niroula, J. M. Pino, C. Roman, M. Schechter, P. E. Siegfried, B. G. Tiemann, C. Volin, J. Walker, R. Shaydulin, M. Pistoia, S. A. Moses, D. Hayes, B. Neyenhuis, R. P. Stutz, and M. Foss-Feig, *The computational power of random quantum circuits in arbitrary geometries* (2024), [arXiv:2406.02501](https://arxiv.org/abs/2406.02501) [quant-ph].
- [58] M. Cetina, L. Egan, C. Noel, M. Goldman, D. Biswas, A. Risinger, D. Zhu, and C. Monroe, Control of transverse motion for quantum gates on individually addressed atomic qubits, *PRX Quantum* **3**, 010334 (2022).
- [59] S. Crain, C. Cahall, G. Vrijsen, E. E. Wollman, M. D. Shaw, V. B. Verma, S. W. Nam, and J. Kim, High-speed low-crosstalk detection of a 171yb+ qubit using superconducting nanowire single photon detectors, *Commun Phys* **2**, 1 (2019).
- [60] C. Roman, A. Ransford, M. Ip, and W. C. Campbell, Coherent control for qubit state readout, *New J. Phys.* **22**, 073038 (2020).
- [61] R. Noek, G. Vrijsen, D. Gaultney, E. Mount, T. Kim, P. Maunz, and J. Kim, High speed, high fidelity detection of an atomic hyperfine qubit, *Opt. Lett., OL* **38**, 4735 (2013).
- [62] J. M. Pino, J. M. Dreiling, C. Figgatt, J. P. Gaebler, S. A. Moses, M. Allman, C. Baldwin, M. Foss-Feig, D. Hayes, K. Mayer, *et al.*, Demonstration of the trapped-ion quantum ccd computer architecture, *Nature* **592**, 209 (2021).
- [63] S. Huang, K. R. Brown, and M. Cetina, Comparing shor and steane error correction using the bacon-shor code, *Science Advances* **10**, eadp2008 (2024).